Stokesian peristaltic pumping in a three-dimensional tube with a phase-shifted asymmetry

Vivian Aranda,[1] Ricardo Cortez,[2] and Lisa Fauci[2]
[1]*Department of Mathematics, Universidad Técnica Federico Santa María, Avenida España 1680, Valparaíso, Chile*
[2]*Department of Mathematics, Tulane University, 6823 St. Charles Avenue, New Orleans, Louisiana 70118, USA*

Many physiological flows are driven by waves of muscular contractions passed along a tubular structure. This peristaltic pumping plays a role in ovum transport in the oviduct and in rapid sperm transport through the uterus. As such, flow due to peristalsis has been a central theme in classical biological fluid dynamics. Analytical approaches and numerical methods have been used to study flow in two-dimensional channels and three-dimensional tubes. In two dimensions, the effect of asymmetry due to a phase shift between the channel walls has been examined. However, in three dimensions, peristalsis in a non-axisymmetric tube has received little attention. Here, we present a computational model of peristaltic pumping of a viscous fluid in three dimensions based upon the method of regularized Stokeslets. In particular, we study the flow structure and mean flow in a three-dimensional tube whose asymmetry is governed by a single phase-shift parameter. We view this as a three-dimensional analog of the phase-shifted two-dimensional channel. We find that the maximum mean flow rate is achieved for the parameter that results in an axisymmetric tube. We also validate this approach by comparing our computational results with classical long-wavelength theory for the three-dimensional axisymmetric tube. This computational framework is easily implemented and may be adapted to more comprehensive physiological models where the kinematics of the tube walls are not specified a priori, but emerge due to the coupling of its passive elastic properties, force generating mechanisms, and the surrounding viscous fluid. © *2011 American Institute of Physics.*
[doi:10.1063/1.3622319]

I. INTRODUCTION

The transport of fluid due to waves of contractions passed along a tube is prevalent in many physiological systems. In particular, mammalian reproduction relies upon peristaltic pumping of both the uterus and the oviducts (fallopian tubes).[1] Peristaltic motion of the walls of the oviduct, along with ciliary beating, are essential for ovum transport. Uterine peristalsis is responsible for rapid sperm transport through the uterus toward the oviduct, the site of fertilization. In addition, muscular contractions of the uterine walls also create the flow field in which the fertilized ovum is passively transported to the site of implantation.

Motivated in part by these physiological flows, there have been many analytic and numerical investigations of the fluid dynamics of peristalsis in two-dimensional channels and three-dimensional tubes. Classical analytical models assumed that the flow was inertia-free, and that the channel or tube walls supported an infinite train of small amplitude sine waves whose wavelengths were long compared to the diameter of the conduit.[2,3] These early studies, for both two-dimensional channels and axisymmetric three-dimensional tubes, examined the mean flow rate induced by the wavetrain, and elucidated the feature of bolus formation in the wave frame when the conduit was sufficiently occluded. This bolus was transported with the wave in the laboratory frame, trapping fluid particles that circulated within it. More recent analytical and numerical investigations extended our understanding of peristalsis by including non-zero Reynolds

number dynamics,[4] transport in finite tubes,[5] the transport of solid particles,[6] the effects of viscoelasticity,[7,8] and the investigation of optimal channel shapes for pumping fluid.[9] In addition, methods of dynamical systems have been used to investigate the topology of flow structures in axisymmetric tubes.[10]

During the secretory phase, when the embryo enters the uterus, asymmetric contractions have been observed in vivo.[11] In an effort to understand the effect of asymmetry on the fluid motion in the uterus, Eytan and Elad[12] used lubrication theory to study the flow patterns in a two-dimensional peristaltic channel with a phase shift between the walls. They demonstrated that the maximum flow rate is achieved when the channel was symmetric about its centerline, and that bolus formation was also possible in asymmetric channels. Previous numerical simulations of flow in asymmetric peristaltic channels, in both the Stokes and non-zero Reynolds number regime, show similar streamline patterns.[13,14]

While the asymmetric peristaltic channel in two dimensions has been well-studied, peristalsis in non-axisymmetric, three-dimensional tubes has received much less attention. Usha and Rao[15] did investigate the peristaltic pumping of a fluid in a pipe of elliptic cross sections, using long wavelength and low Reynolds number assumptions. Under these assumptions, they calculated that the flow rate increased with a decrease in eccentricity of the elliptic cross sections, and was maximal in the axisymmetric case.[15] Each elliptic cross section of the tubes considered had its major axis aligned with the same direction. Here, we investigate

peristaltic flow induced by a different sort of axial asymmetry in a tube by introducing a phase-shift parameter. We view this as a three-dimensional analog of the two-dimensional channel model with a phase shift between the motility of opposite walls.

We assume that the length and velocity scales of the peristaltic tube are such that the fluid is governed by the Stokes equations of zero Reynolds number flow. In addition, as we are motivated by the uterine and oviductal systems, we wish to capture the flow in tubes whose wavelengths are considerably larger than the average cross sectional diameter of the tube. We use the method of regularized Stokeslets[16,17] to determine the flow generated by a distribution of regularized forces on the tube surface. This numerical approach is grid-free in the sense that the fluid region within the tube does not require an underlying mesh. Along with our investigation of the flow in the phase-shifted tube, we also demonstrate the validity of this numerical method by comparing the flow structures and mean flows calculated with those predicted by the classical theory for the three-dimensional axisymmetric tube. We note that although the focus of this paper is on tubes with long wavelengths, this is not a restriction of the method.

II. METHODS

A. Phase-shifted tube geometry

Our goal is to introduce asymmetry into the tube using a single phase-shift parameter. We do this by considering a finite tube whose longitudinal axis is the segment $0 \leq x \leq \Lambda$ and whose cross sections, for a fixed value x, are the ellipses

$$\left(\frac{y}{r_a(x,t)}\right)^2 + \left(\frac{z}{r_b(x,t)}\right)^2 = 1 \qquad (1)$$

where

$$r_a(x,t) = r_o + a\sin\left(\frac{2\pi}{\lambda}(x - ct) + \beta\right), \qquad (2)$$

$$r_b(x,t) = r_o + a\sin\left(\frac{2\pi}{\lambda}(x - ct)\right). \qquad (3)$$

Here, λ is the wavelength, c is the wave speed, r_o is the average tube radius, and a is an amplitude parameter, $a \leq r_o$. The occlusion ratio will be denoted by $\chi = a/r_o$. We choose $\Lambda = M\lambda$ to be an integer number of wavelengths. We note the following:

- All cross sections are ellipses whose major and minor axes are always aligned with the y and z axes. The parameter β represents a phase shift between the sinusoidally varying lengths of these major and minor axes.
- When the phase shift $\beta = 0$, the lengths of the major and minor axes are equal for all time ($r_a(x,t) = r_b(x,t)$), and all cross sections are circles, representing the axisymmetric case, as depicted in Figure 1(a).
- For fixed values of t and β, the major axis of the cross sections is aligned with the y direction for some values of x and aligned with the z direction for other values of x, depending on whether $r_a(x,t) > r_b(x,t)$. Necessarily, there will be two values of x per spatial period where the cross section is circular.
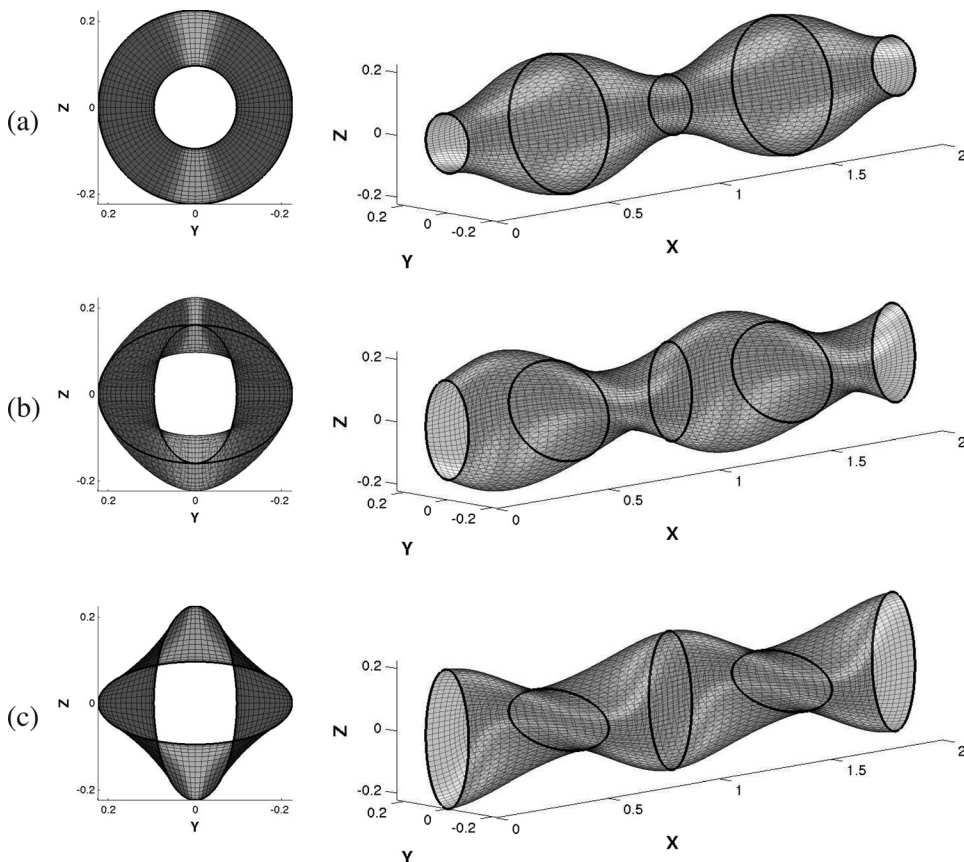

FIG. 1. The geometry of the tube at $t = .25$ for (a) $\beta = 0$, (b) $\beta = \pi/2$, and (c) $\beta = \pi$. Here, each tube supports two wavelengths and has an occlusion ratio of $\chi = a/r_0 = 0.6$. The thick elliptic lines indicate cross sections of the tube at a fixed position of x. Note that these cross sections remain orthogonal to the x-axis for all t. The left column shows the projected cross sections when looking down through the tube.

Tube geometries for $\beta = \pi/2$ and π are shown in Figures 1(b) and 1(c), respectively. The left column of the figure shows the projections of the cross sections of each of the three tubes when looking down through the tube along the x-axis. One can see that the smallest and largest radii of the circular cross sections in the axisymmetric case correspond to $r_o + a$ and $r_o - a$, the extreme lengths of the minor and major axes of the elliptical cross sections in the non-zero β cases. A perspective view and the projection of various cross sections are shown in Figures 2(a) and 2(b), respectively. Notice that the cross sectional area varies significantly with x.

Since we are considering a tube that supports an integral number of wavelengths, the total volume of the tube remains constant as the wave passes along it. However, the volume of the tube depends upon the phase shift β and the occlusion ratio χ. The volume of a single wavelength of the tube is

$$V(\beta, \chi) = \pi r_o^2 \, \lambda \left(1 + \frac{\chi^2}{2} \cos(\beta) \right). \tag{4}$$

Even with a non-zero phase shift β, we may still define a wave frame in which the flow is steady. The transformation from the laboratory frame to this wave frame is given by

$$x^* = x - ct$$
$$y^* = y$$
$$z^* = z.$$

Below we will examine how the phase-shift parameter β affects the overall mean flow achieved by the pumping, along with the related flow structures in the wave frame.

B. Governing equations and boundary conditions

The flow is described by the steady Stokes equations

$$0 = \nabla p + \mu \Delta \vec{u} + \vec{F}(\vec{x}, t) \tag{5}$$
$$0 = \nabla \cdot \vec{u} \tag{6}$$

where μ is the fluid viscosity, p is the pressure, $\vec{u}$ is the fluid velocity, and $\vec{F}$ is the external force per unit volume applied to the fluid. This external force field represents the force of the tube walls on the fluid. The tube is of finite extent, open at each end, and its surface acts as a source of forces in the fluid domain, which is all of $\mathbb{R}^3$. In this unbounded domain, we enforce the condition that the velocity decays at infinity. Here, it is assumed that there is no imposed pressure drop along the tube. We note that most of the classical theory of peristalsis is for periodic tubes of infinite extent. However, below we will compare our calculations with those for a periodic axisymmetric tube, because it has been shown that pumping performance is independent of tube length if there is an integral number of waves along the tube.[5]

C. Numerical solution: Regularized Stokeslet formulation

The objective of this study is to describe a model of peristalsis in three dimensions for both axisymmetric and non-axisymmetric tubes. We use the method of regularized Stokeslets (MRS),[16,17] which is appropriate for the computation of Stokes flows driven by external forces. The MRS has been used extensively for the study of related problems in micro-organism motility and bacterial processes (e.g., Refs. 18–24).

The MRS replaces a Dirac delta distribution of surface forces with a regularized force field using basis functions ϕ_δ centered at discrete points on the surface.[16,17] Given N points $\vec{x}_k(t)$ discretizing the tube surface at time t and the force

$$\vec{F}(\vec{x}, t) = \sum_{k=1}^{N} \vec{f}_k(t) \phi_\delta(\vec{x} - \vec{x}_k(t)), \tag{7}$$

the pressure and velocity at any point $\vec{x}$ are given by

$$p(\vec{x}, t) = \sum_{k=1}^{N} \vec{f}_k(t) \cdot \nabla G_\delta(\vec{x} - \vec{x}_k(t)), \tag{8}$$

$$\vec{u}(\vec{x}, t) = \frac{1}{\mu} \sum_{k=1}^{N} \left\{ (\vec{f}_k(t) \cdot \nabla) \nabla B_\delta(\vec{x} - \vec{x}_k(t)) \right. $$
$$\left. - \vec{f}_k(t) \cdot G_\delta(\vec{x} - \vec{x}_k(t)) \right\}. \tag{9}$$

The functions G_δ and B_δ satisfy $\Delta G_\delta = \phi_\delta$ and $\Delta B_\delta = G_\delta$, and are completely determined by the blob used. Here, we choose the blob used in Refs. 16, 17
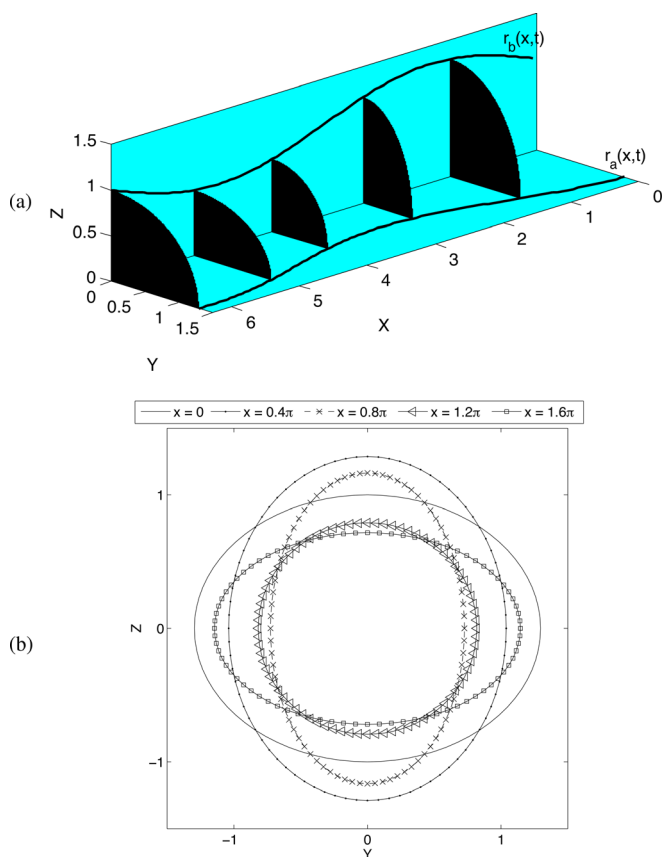

FIG. 2. (Color online) Depiction of selected tube cross sections at various locations along one spatial period. The parameters used were $r_0 = 1$, $a = 0.3$, $\lambda = 2\pi$, $\beta = 0.55\pi$, and $t = 0$. All cross sections are ellipses with major and minor axes aligned with the y and z axes. Panel (a) shows a perspective view displaying the cross sections in one quadrant as well as the functions $r_a(x, t)$ and $r_b(x, t)$ in Eqs. (2)–(3). Panel (b) shows the indicated cross sections viewed from one end of the tube.

$$\phi_\delta(\vec{x} - \vec{x}_k) = \frac{15 \, \delta^4}{8\pi \big(\| (\vec{x} - \vec{x}_k) \|^2 + \delta^2 \big)^{7/2}}. \qquad (10)$$

Equation (9), when evaluated at all N points that discretize the tube surface, must give the prescribed peristaltic velocity $\vec{u}(\vec{x}_k(t), t)$, which can be easily arrived at by differentiation of Eqs. (2)–(3). The velocity specification at each of these N surface points yields a linear system of $3N$ equations for the unknown forces $\vec{f}_k(t)$ that must be applied at those points to achieve the specified velocities. Once the forces are found by solving the linear system, Eq. (9) may be applied directly to evaluate the fluid velocity at any point $\vec{x}$ of interest. In particular, by evaluating the fluid velocity within cross sections of the tube, we approximate the mean flow rate.

D. Computing the flow rate

The computation of the instantaneous flow rate involves the numerical evaluation of

$$q(x, t) = \int_{A(x,t)} u(x, y, z, t) \, dy \, dz$$

where x and t are fixed and $A(x, t)$ is the area inside the ellipse $(y/r_a)^2 + (z/r_b)^2 = 1$. To do this, we first map the area inside the ellipse to the unit disk D_0 via the transformation $(y, z) = (r_a\alpha, r_b\gamma)$, so that

$$q(x, t) = r_a r_b \int_{D_0} u(x, r_a\alpha, r_b\gamma, t) \, d\alpha \, d\gamma. \qquad (11)$$

The unit disk is discretized into N_p patches of equal area by representing the disk as the union of N_r concentric annuli of width $h = 1/N_r$. For a fixed $k \in \{1, 2, \ldots, N_r\}$, the area of the annulus $(k - 1)h < r < kh$ equals $h^2\pi(2k - 1)$ so that we choose to place $3(2k - 1)$ points in this annulus at a radial distance $r = h(k - 1/2)$ and equally spaced in θ. The patch of area covered by each point (α_k, γ_k) defined this way is $A = (\pi/3)h^2$, regardless of k. The distribution of points within the unit disk is displayed in Figure 3. For a given number N_r of annuli, the total number of points inside the disk is $N_p = 3N_r^2$. In our computations, we use $N_r = 15$. The integral in Eq. (11) is approximated by the midpoint rule

$$q(x, t) \approx r_a r_b \left(\frac{\pi}{3}\right) h^2 \sum_{m=1}^{N_p} u(x, r_a\alpha_m, r_b\gamma_m, t).$$

Once we have computed the instantaneous flow rate $q(x, t)$, we may average it over one period of time T or we may find the average flow rate per unit length of tube. The time average is computed simply by averaging computed values at discrete times since the flow rate is a periodic function of time. The average flow rate per unit length of tube is computed using the trapezoid rule

$$\bar{q}_T(x) = \frac{1}{T} \int_0^T q(x, t) dt$$

$$\approx \frac{1}{T} \sum_{k=0}^{N_T - 1} q(x, k\Delta t)\Delta t, \qquad (12)$$
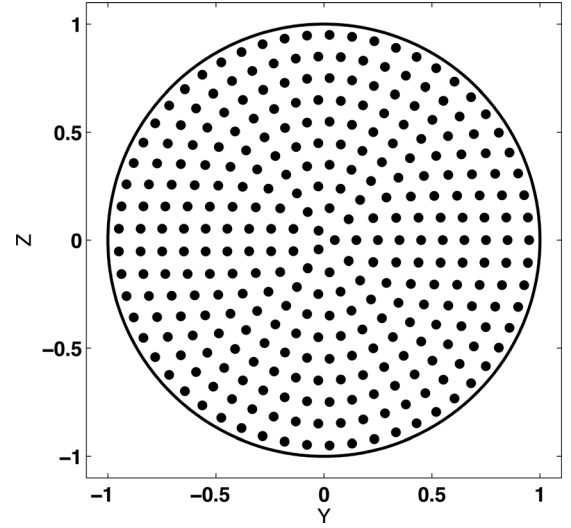

FIG. 3. Discretization of the unit disk for computing the instantaneous flow rate. The disk is represented by N_r annuli of width $h = 1/N_r$. The annulus $(k-1)h < r < kh$ for $k \in \{1, 2, \ldots, N_r\}$ is subdivided into $(6k - 3)$ angular slices so that $\Delta\theta = 2\pi/(6k - 3)$. The quadrature points used in this annulus are of the form $(\alpha, \gamma) = (k - 1/2)h(\cos(n\Delta\theta), \sin(n\Delta\theta))$ for $n = 1, 2, \ldots, (6k - 3)$. The total number of points used is $3N_r^2$, each covering an area of $A = h^2(\pi/3)$.

$$\bar{q}_L(t) = \frac{1}{L} \int_{x_0}^{x_0+L} q(x, t) dx \approx \frac{h}{2L} (q(x_0, t)$$

$$+ q(x_0 + L, t) + 2 \sum_{j=1}^{M_L - 1} q(x_0 + jh, t)), \qquad (13)$$

with $\Delta t = T/N_T$ and $h = L/M_L$, where N_T is the number of quadrature points in a time period, and M_L is the number of quadrature points per wavelength. The results of this section were obtained with $N_T = 20$ and $M_L = 40$.

III. RESULTS

Motivated by uterine peristalsis,[25] we choose the tube geometry whose parameters are given in Table I. The tube supports two wavelengths, has a radius $r_0 = 0.08\lambda$, and undergoes oscillations with temporal period $T = \lambda/c$. We choose these as baseline parameters, and will examine the pumping that results when varying the occlusion ratio $\chi = a/r_0$ and the value of the asymmetry parameter β. This model problem will allow direct comparison between computed flow rates and streamlines with those predicted by classical analysis in the case of axisymmetric tubes. In addition, we will use the asymptotic value of flow rate to

TABLE I. Model parameters.

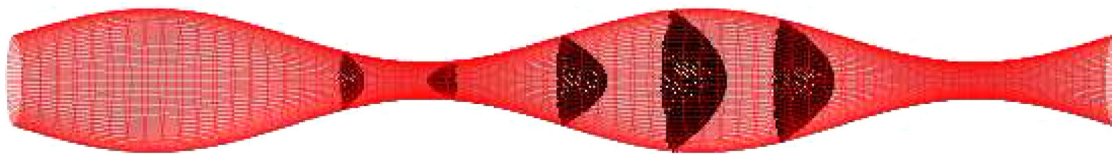|	Symbol	Units	Value
Wavelength	λ	mm	25.0
Tube radius	r_o	mm	2.0
Wave speed	c	mm/s	1.25
Viscosity	μ	gr/mm s	0.001
Frequency	f	1/s	0.05
Period	$T = 1/f$	s	20
Channel length	$\Lambda = 2\lambda$	mm	50

FIG. 4. (Color online) Example of computed flow profiles in the axisymmetric tube at various cross sections. The Stokeslet strengths are first computed based on velocity boundary conditions on the surface of the tube. Then, the instantaneous flow at various cross sections is computed and displayed here as surfaces (approximate paraboloids) inside the tube. The figure shows that while the net flow is from left to right, there are sections of the tube where the flow is in the opposite direction.

calibrate our choice of the numerical regularization parameter δ with respect to the spacing Δs between discrete points that resolve the tube surface.

In general, the time-averaged flow rate Q through a cross section of the tube at $x = x_l$ is defined by

$$Q(x_l) = \frac{1}{T} \int_0^T \int_{A(x_l,t)} u(x_l, y, z, t) \, dy dz \, dt \qquad (14)$$

where u is the axial component of velocity and $A(x_l, t)$ is the tube's cross-sectional area at $x = x_l$ at time t. Since the total tube volume depends on χ and β, for the purpose of comparison, it is best to non-dimensionalize the mean flow rate by the tube volume divided by the time period

$$\bar{Q}(x_l) = \frac{Q(x_l)}{V(\beta, \chi)/T}. \qquad (15)$$

A. Axisymmetric tube

We first focus our attention on the axisymmetric tube with $\beta = 0$, for which asymptotic results in the long-wavelength limit are available. In this case, the dimensional mean flow rate was computed by Shapiro et al.[3] to be

$$Q_{theory} = (\pi \, r_o^2 \, c) \, \frac{4\chi^2 \left(1 - \frac{\chi^2}{16}\right)}{\left(1 + \frac{3\chi^2}{2}\right)}.$$

Using our normalization factor in Eq. (15), the dimensionless asymptotic mean flow rate becomes

$$\bar{Q}_{theory} = \frac{1}{\left(1 + \frac{\chi^2}{2}\right)} \frac{4\chi^2 \left(1 - \frac{\chi^2}{16}\right)}{\left(1 + \frac{3\chi^2}{2}\right)}. \qquad (16)$$

We note that although our tube is finite, since we constrain it to support an integral number of wavelengths, we can compare our calculations with the analytical solutions for an infinite periodic tube.[5]

As an example of a long wavelength tube, we use a geometry based on Eq. (1) with $r_0/\lambda = 0.08$ (see Figure 4). We discretize the surface of the tube by dividing it into N_C cross sections with NP_j points around each circular cross section, $j = 1, 2, \ldots N_C$. This is done in such a way as to keep the average distance Δs between surface points constant. Since we are prescribing the kinematics of the surface points on the tube, at

any given time t we know the velocities at each of these points. The forces on the tube surface and the internal fluid velocity are computed as described in Sec. II. Figure 4 shows a snapshot of several flow profiles in the laboratory frame along a cross section of the axisymmetric tube with occlusion ratio $\chi = 0.3$. As the surface wave is moving to the right, we see that the profiles are largely pointing toward the right, except in the occluded cross sections, where the flow is reversed.

In order to compute the mean flow rate achieved by the pumping, we evaluate the fluid velocities at discrete points within the circular cross sections at a few fixed stations along the length of the tube. While the values of the time-averaged flow over one period at different cross sections would necessarily be the same in an infinite tube due to conservation of mass, the values in the finite tube do not have the same restriction. Figure 5 shows the time-averaged flow rate as a function of axial location for tubes that are 2- and 3-wavelengths long. The horizontal line is the asymptotic mean flow rate in Eq. (16). The figure shows that our computed values are approximately constant at cross sections away from the ends of tube. Our computed mean flow rate Q_{St} is the space average (using Eq. (13)) of these time-averaged flow rates. The figure shows that the largest difference between the computed flow rates and the asymptotic one is about 5.4% (for 2 wavelengths) and 6.6% (for 3 wavelengths).

While the time-averaged flow rates are roughly constant, the instantaneous flow rates for a given value of t vary significantly along the tube length. Figures 6(a) and 6(b) show instantaneous flow rates as functions of axial position at $t = 0$ for tubes that are 2- and 3-wavelengths long, respectively. The solid horizontal line is the asymptotic theory mean flow rate. The dashed horizontal lines are the space average of the oscillating functions over their respective domains computed with Eq. (13) at $t = 0$ only. If we evaluated this space average at several values of t over a period, we would arrive at the space-averaged flow rate as a function of time shown in Figures 7(a) and 7(b). Note that the space average over the entire tube shows more variation than the space-average over the middle tube wavelength only. Also, the space averages show less variation in time when the tube length is three wavelengths rather than two. In either case, however, the variations are due to the open ends of the tube.

For the model problem with $\chi = 0.3$, the asymptotic mean flow rate given by Eq. (16) is $\bar{Q}_{theory} = 0.3018$. For instance, for this model problem, we choose 9 flow meters spaced in the middle half of the tube, and compute the time-averaged flow through each section. We take this value as the reference mean flow rate of pumping, and compare our
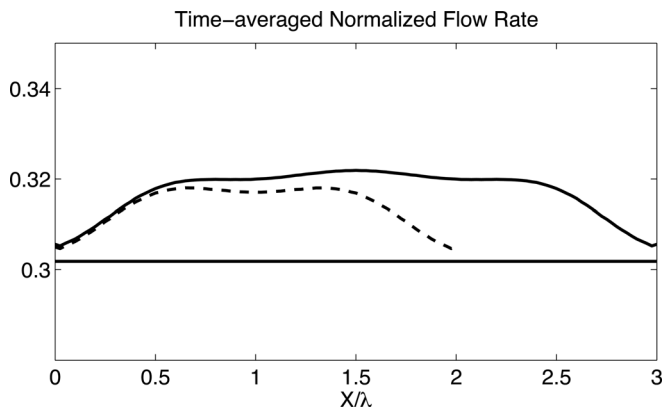
FIG. 5. Flow rate averaged over one temporal period as a function of axial position in the tube, $\bar{q}_T(x)$. The figure shows the result for cases when the tube is 2 and 3 wavelengths long. The cross-sections near the center of the finite tube show a time-average flow rate that is approximately constant while the cross-sections near the endpoints of the tube show the effect of the open ends of the tube. The horizontal line shows the average flow rate given by the asymptotic theory for an infinite periodic tube of small aspect ratio. The largest difference between the computed flow rates and the asymptotic one is about 5.4% (for 2 wavelengths) and 6.6% (for 3 wavelengths).

computed mean flow rate for given surface discretizations Δs and regularization parameters δ. As discussed in Ref. 17, this blob parameter (for the blob function in Eq. (10)) is best taken to be comparable to the spacing between the discrete points that discretize the surface. Figure 8(a) shows the relative difference between $\bar{Q}_{theory}$ given in Eq. (16) and the computed mean flow $\bar{Q}_{St}$ as a function of $\delta/\Delta s$ for three different surface discretizations $\Delta s = 0.5$, 0.4, and 0.3 mm. We see that, for a given surface discretization a very small regularization parameter, relative to the spacing between discrete surface points, results in an underresolved tube surface, and leads to relative errors as high as 25%. Similarly, regularization parameters that are large compared to the spacing between discrete surface points result in a smeared force distribution at the surface that is of too wide an extent. We can deduce that the optimal choice of regularization parameter for this problem is $\delta = \Delta s$. In fact, for $\delta = \Delta s = 0.3$ mm, the computed dimensionless mean flow rate is $\bar{Q}_{St} = 0.3021$, which compares very well with the asymptotic theory.

Figure 8(b) compares the computations of the mean flow as a function of the amplitude ratio $\chi = a/r_o$ with those predicted from Eq. (16). Here, we chose $\delta = \Delta s$, with a surface discretization of $\Delta s = 0.28$ mm. Note that even though the analysis giving rise to $\bar{Q}_{theory}$ assumed small amplitude oscillations, flow rates at larger occlusion ratios, even $\chi = 0.9$, agree very well with the computations that carry no such assumption.

The long wavelength theory of Shapiro et al.[3] also included the calculation of the stream function in the steady wave frame for the axisymmetric tube. In Figures 9(a) and 9(c), we plot the level curves of this stream function for the occlusion ratio $\chi = 0.3$ and $\chi = 0.6$, respectively. These should be compared to Figures 9(b) and 9(d) that show the corresponding wave frame streamlines computed using the method of regularized Stokeslets. For these occlusion ratios of $\chi = 0.3$ and $\chi = 0.6$, bolus formation is achieved. We see that the larger occlusion ratio results in a bolus of larger extent than in the less occluded channel, which supports more streamlines near the walls where particles are not trapped, but carried along by the flow in this wave frame.

B. Non-axisymmetric tube

We now examine the characteristics of pumping in the phase-shifted tube ($\beta \neq 0$). Although our model is not restricted to the long wavelength regime, we again choose the baseline parameters as in Table I above, but this time allow for a non-zero phase shift β. We first examine the efficacy of pumping as a function of β. Figure 10 shows the computed normalized mean flow rate as a function of the phase shift parameter β for the occlusion ratios $\chi = 0.3$ and $\chi = 0.6$. We see that, in each case, the maximum mean flow is achieved in the axisymmetric case $\beta = 0$, and that it decreases monotonically as the phase shift increases toward its maximal deviation from axial symmetry at $\beta = \pi$. The difference in flow rate as asymmetry increases is more pronounced for the larger occlusion, showing more than a seven-fold decrease.

This result is a three-dimensional analog of that found in the two-dimensional phase-shifted channel analyzed by Eytan and Elad.[12] They demonstrated that the maximal flow
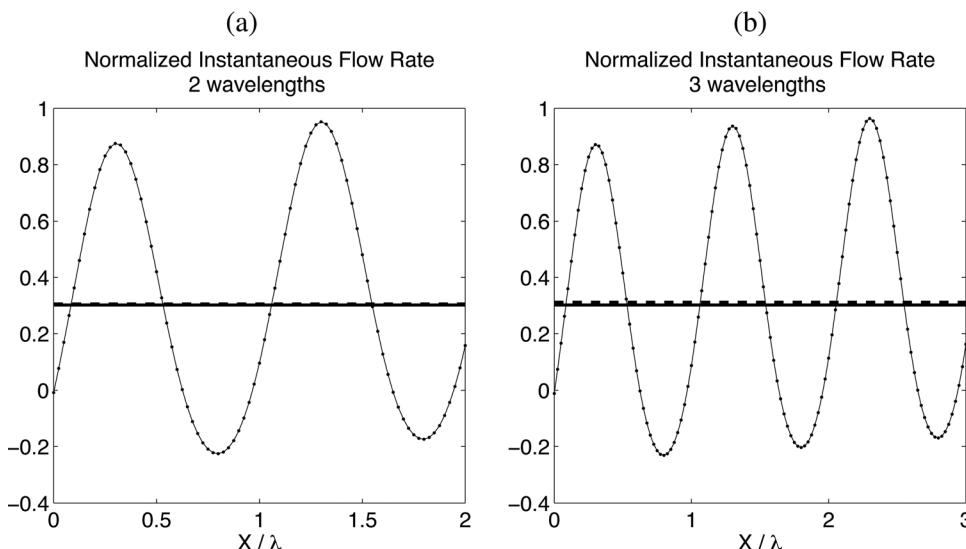

FIG. 6. Instantaneous flow rate at $t = 0.05$ as a function of axial position in the tube. Panel (a): A tube of 2 wavelengths. Panel (b): A tube of 3 wavelengths. In both cases, the solid horizontal line is the theoretical asymptotic value 0.30181 and the horizontal dashed line is the average flow rate in the tube computed by integrating in x. The value in panel (a) is 0.30575 and in panel (b) it is 0.31154. The parameters used were $\Delta s \approx 0.49$, $\chi = 0.3$, and $\delta = \Delta s$.

(a)

Tube–averaged Normalized Flow Rate
2 wavelengths

(b)

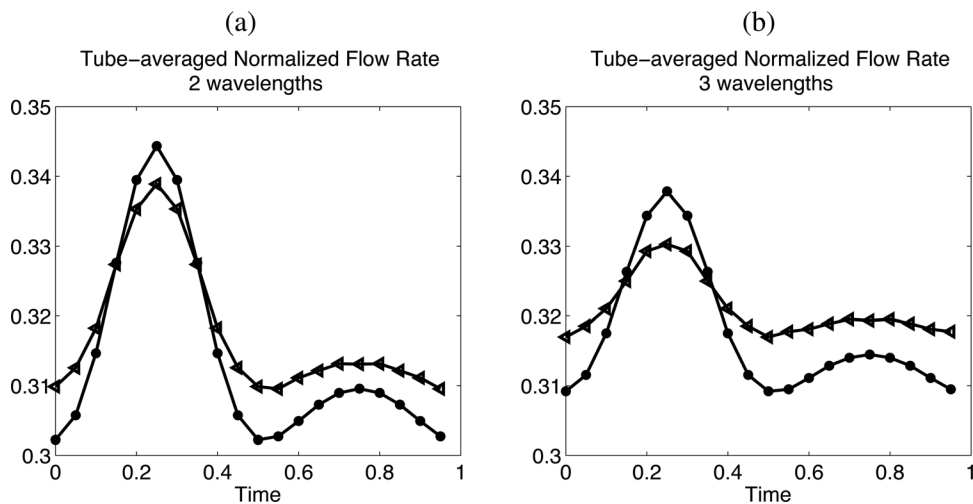Tube–averaged Normalized Flow Rate
3 wavelengths

FIG. 7. Average flow rate per unit length of the tube as a function of time over one period, $\bar{q}_L(t)$. The curve with dots in panel (a) shows the result when the tube is 2 wavelengths long. The curve with dots in panel (b) shows the result when the tube is 3 wavelengths long. The time discretization is $\Delta t = 0.05$ dimensionless units. In both panels, the curves with triangles show the same average flow rate per unit length of the tube when only a single wavelength in the middle of the tube is considered in order to reduce end-tube effects. The parameters used were $\Delta s \approx 0.49$, $\chi = 0.3$, and $\delta = \Delta s$.

rate is achieved for the channel that is symmetric about its centerline, and is actually zero when the walls of the channel oscillate in parallel. In the latter case, the streamlines are shown to have no component in the direction of pumping. In our three-dimensional case, there is no value of β where all cross sections have the same area, so the mean flow is non zero in each case.

In order to gain some insight into our three-dimensional case, we examine wave frame particle trajectories within the axisymmetric tube for $\chi = 0.6$ (Figure 11) and compare these to wave frame particle trajectories for $\beta = \pi/2$ (Figure 12). While we see particles circulating with a bolus in both cases, the closed wave frame streamlines in the axisymmetric case lie within a plane with a fixed angle about the axis of symmetry. This is especially evident in Figure 11(c) that shows the linear projections of the particle paths when looking down through the tube axis. This angular symmetry is not observed in the wave frame streamlines of the phase-shifted tube in Figure 12(c). Here, we see that as the particles circulate, they also exhibit drift in the angular direction.

We also illustrate the angular dependence of the wave frame streamlines for $\beta = \pi/2$ in Figures 13(a)–13(e). Each frame shows the two-dimensional streamlines of the flow computed by projecting the wave frame velocity field onto a plane with a fixed angle about the centerline of the tube. (If this were the $\beta = 0$ axisymmetric case, each of the frames would be identical.) Note that each frame does show a bolus,

and the center of the bolus occurs at the same cross-sectional value of x. However, the walls of the tube are not the same in each plane, and exhibit crests at different locations with respect to the bolus center. In addition, the shape of the bolus is also different in the various planes. We also note that because these are projected two-dimensional streamlines of the full three-dimensional flow, some of the streamlines do not remain within the projected tube boundaries.

IV. DISCUSSION

The MRS is based upon the linear relationship between forces applied at discrete points in three-space and the fluid velocities at those points in an unbounded viscous fluid. The errors in the computation of Stokes flow using the MRS are of two types: (1) the discretization error due to the approximation of a continuous surface (i.e., the tube walls) by discrete points and (2) the regularization error due to the parameter δ that replaces a point force by a regularized force. It was shown in Ref. 17 that the regularization error is $O(\delta)$ in a region of size $O(\sqrt{\delta})$ surrounding the surface, but the error improves to $O(\delta^2)$ away from the surface. Moreover, it was also shown in Ref. 17 that the discretization error is $O(\Delta s^2)$, where Δs is the average distance between points that discretize the surface.

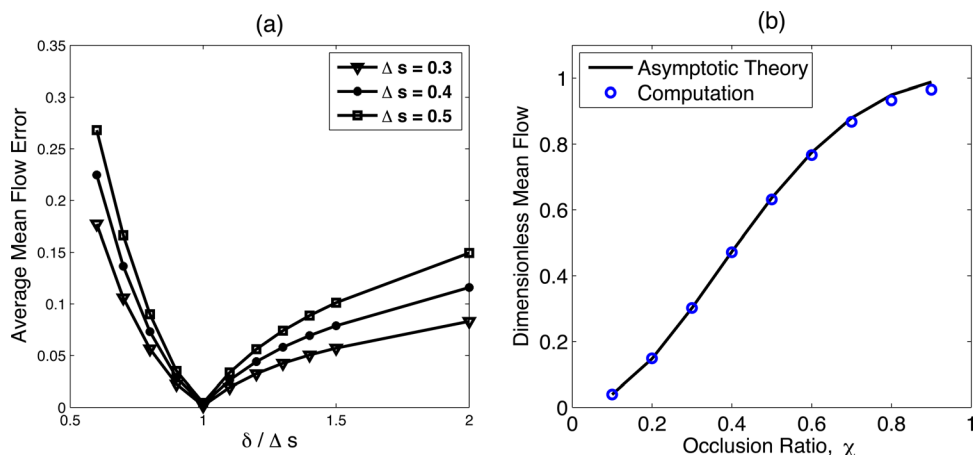In this study, we have considered the flow due to peristalsis where the kinematics of the tube surface were

(a)

(b)

FIG. 8. (Color online) Panel (a) shows the relative error in the mean flow computations, $||\bar{Q}_{theory} - \bar{Q}_{St}||/||\bar{Q}_{theory}||$, for three different surface discretizations as a function of the constant of proportionality between the blob size and the surface discretization $\delta/\Delta s$. Panel (b) shows the dimensionless mean flow as a function of the occlusion ratio χ arrived at by the theory in Shapiro *et al*. (see Ref. 3) (continuous curve), and regularized Stokeslet computations (discrete points).
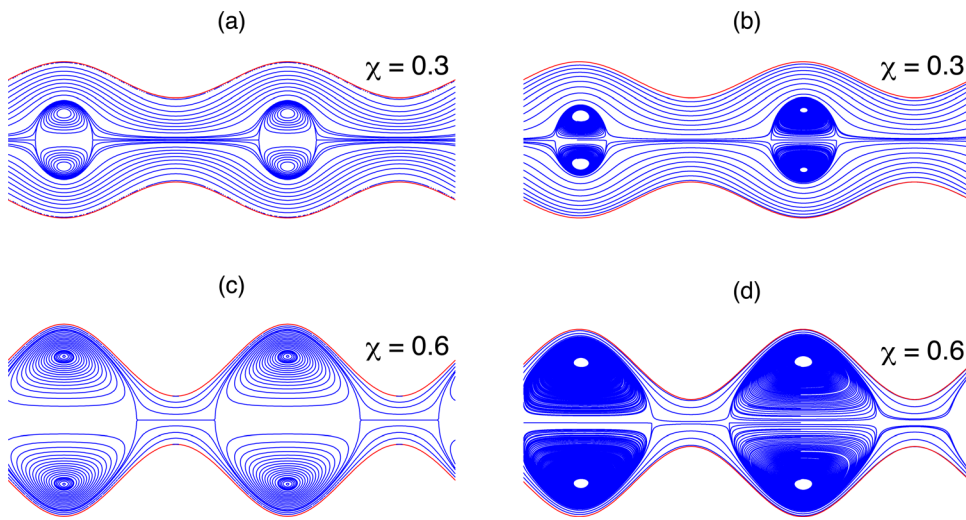
FIG. 9. (Color online) Waveframe streamlines in the axisymmetric tube. The level curves of the stream function arrived at using long wavelength theory (see Ref. 3) for $\chi = 0.3$ are shown in panel (a), and for $\chi = 0.6$ in panel (c). The streamlines computed using the method of regularized Stokeslets (Ref. 16) for $\chi = 0.3$ are shown in panel (b), and for $\chi = 0.6$ in panel (d). We have expanded the scale in the y-direction for clarity.
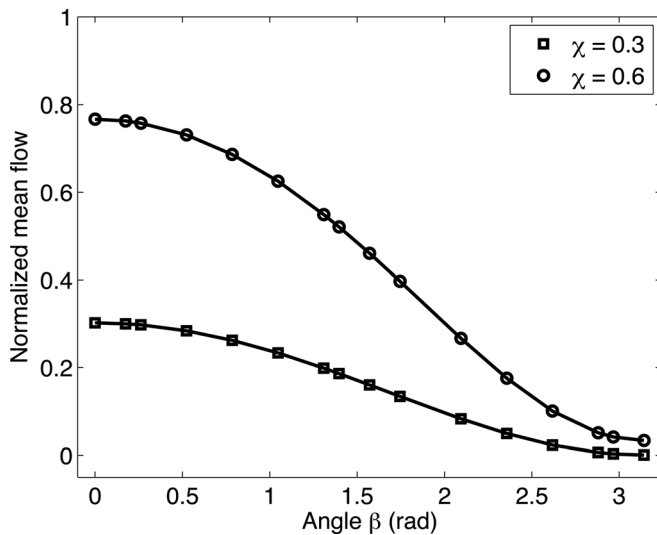

FIG. 10. Normalized mean flow rate versus β for occlusion ratio $\chi = 0.3$ and $\chi = 0.6$.

prescribed. Using these specified velocities at discrete points of the tube surface, we solved for the forces at these discrete points that were required to produce these velocities. Once these forces were known, the fluid velocity within the tube was calculated, and the flow features of peristalsis were measured. The results presented indicate the effectiveness of this approach, and also provide insight into the flow dynamics in a tube with a phase-shifted asymmetry.

Conversely, the linear relationship between forces and velocities in Stokes flow may also be exploited to compute velocities at discrete points on a surface due to specified forces applied at these points. Therefore, this framework is ideally suited to solve the full fluid-structure interaction problem where forces due to passive elasticity of the tube and active bending moments induce the flow, and the geometry of the tube emerges from the resulting velocity. The input to such an integrative model of uterine peristalsis would be the elastic moduli of the fibers that build the uterine surface, and a model of smooth muscle contraction in the cells along these fibers. For instance, in future work, we hope to
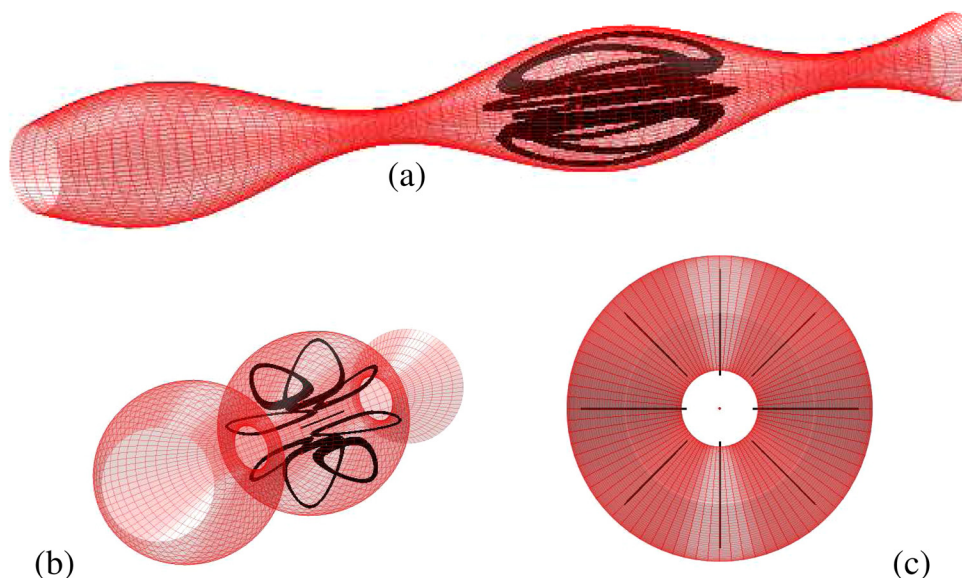

FIG. 11. (Color online) Axisymmetric tube showing wave frame streamlines traced out by some particle trajectories. These computed three-dimensional streamline patterns are depicted from different perspectives. Panel (b) shows a perspective at a small angle from the tube axis while panel (c) shows the particle paths when looking down through the tube axis. Note that the particles show periodic motion on planes containing the tube axis. Here, $\chi = 0.6$ and $\beta = 0$.
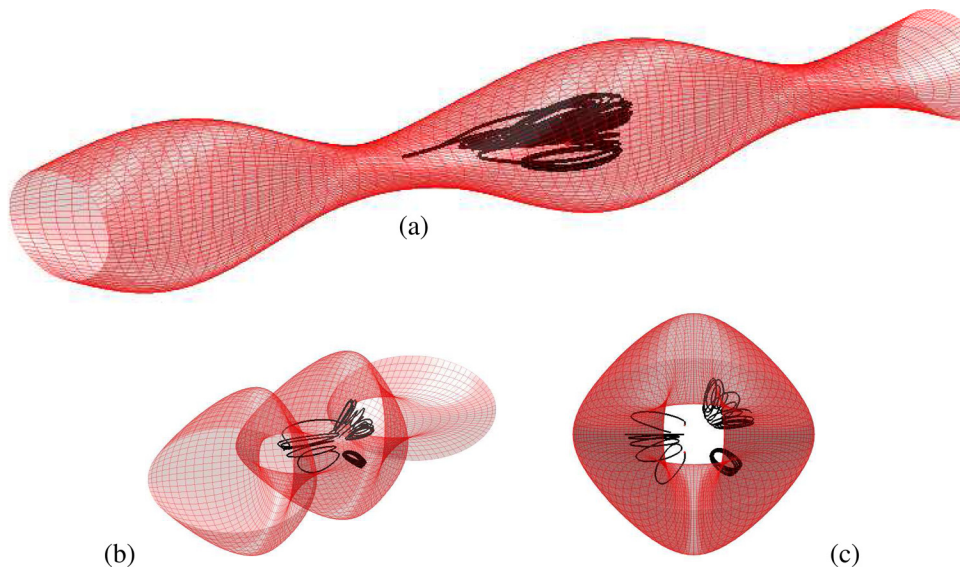
FIG. 12. (Color online) Non-axisymmetric tube showing wave frame streamlines traced out by some particle trajectories. Panel (b) shows a perspective at a small angle from the tube axis while panel (c) shows the particle paths when looking down through the tube axis. Note that the particles display rotations inside a bolus and a drift in the angular direction. Here, $\chi = 0.6$ and $\beta = \pi/2$.

incorporate the model of excitation-contraction in a single uterine myocyte, based upon intra-cellular calcium dynamics, that was presented in Ref. 26. The regularized Stokeslet formulation and the closely related immersed boundary formulation of an actuated elastic object interacting with an incompressible fluid in a non-zero Reynolds number flow (e.g., Ref. 27) have been used successfully in other integrative models in biofluiddynamics, such as the dynein-induced beating of cilia,[28] bacterial flagellar bundling,[29] and a neuromechanical model of lamprey swimming.[30]

Here, we chose to study a three-dimensional peristaltic tube with open ends. Of course, the uterine cavity is closed at the fundal end. In numerical computations in a two-dimensional model of a uterine channel closed at one end, Yaniv *et al.*[31] have shown that the resulting flow field and particle trajectories are tremendously different from the corresponding dynamics in a periodic or open-ended channel. Cellular flow structures that confined individual fluid particles were observed. We plan to extend our model of peristalsis to examine the effect of a closed end in a three-dimensional tube.

V. CONCLUSION

We have presented an investigation of peristaltic pumping of a viscous fluid in a non-axisymmetric three-dimensional tube. Although there are many ways to introduce asymmetry in tube, we focus on a particular case of a phase-shifted tube, whose asymmetry depends upon a single phase-shift parameter. We view this to be a three-dimensional analog of the phase-shifted two-dimensional channel. As in the two-dimensional case, we find that a tube that is symmetric about its centerline maximizes the fluid pumped in the wave direction. Moreover, we offer validation of our numerical approach, the method of regularized Stokeslets, by comparing the numerical results with the analytical results of flow in a periodic axisymmetric tube that were based upon long wavelength theory. Having an analytic solution to this closely related problem also enabled us to calibrate our choice of numerical parameters.
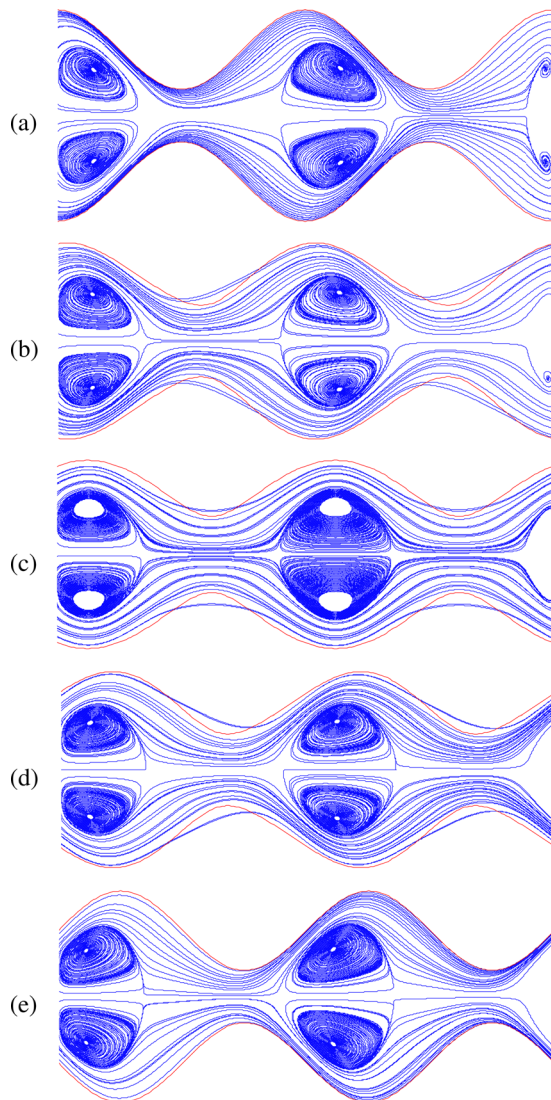

FIG. 13. (Color online) Streamlines for the non-axisymmetric tube projected onto the plane containing the x-axis and the line $y\cos(\theta) + z\sin(\theta)$ for (a) $\theta = 0$, (b) $\theta = \pi/6$, (c) $\theta = \pi/4$, (d) $\theta = \pi/3$, and (e) $\theta = \pi/2$. The values $\beta = \pi/2$ and $\chi = 0.6$ were fixed.

ACKNOWLEDGMENTS

[1] L. Fauci and R. Dillon, Annu. Rev. Fluid Mech. **38**, 371 (2006).

[2] M. Jaffrin and A. Shapiro, "Peristaltic pumping," Annu. Rev. Fluid Mech. **3**, 13 (1971).

[3] A. Shapiro, M. Jaffrin, and S. Weinberg, "Peristaltic pumping with long wavelengths at low Reynolds number," J. Fluid Mech. **37**, 799 (1969).

[4] S. Takabatake, K. Ayukawa, and A. Mori, "Peristaltic pumping in circular cylindrical tubes: A numerical study of fluid transport and its efficiency," J. Fluid Mech. **193**, 267 (1988).

[5] M. Li and J. Brasseur, "Nonsteady peristaltic transport in finite-length tubes," J. Fluid Mech. **248**, 129 (1993).

[6] K. Connington, Q. Kang, H. Viswanathan, A. Abdel-Fattah, and S. Chen, "Peristaltic particle transport using the lattice Boltzmann method," Phys. Fluids **21**, 053301 (2009).

[7] J. Chrispell and L. Fauci, "Peristaltic pumping of solid particles immersed in a viscoelastic fluid," Math. Model. Nat. Phenom. (in press).

[8] J. Teran, L. Fauci, and M. Shelley, "Peristaltic pumping and irreversibility of a stokesian viscoelastic fluid," Phys. Fluids **20**, 073101 (2008).

[9] S. Walker and M. Shelley, "Shape optimization of peristaltic pumping," J. Comp. Phys. **229**, 1260 (2010).

[10] J. Jimenez-Lozano and M. Sen, "Streamline topologies of two-dimensional peristaltic flow and their bifurcations," Chem. Eng. Process.: Process Intensification **47**, 704 (2009).

[11] O. Eytan, I. Halevi, J. Har-Toov, I. Wolman, D. Elad, and A. Jaffa, "Characteristics of uterine peristalsis in spontaneous and induced cycles," Fertil. Steril. **76**, 337 (2001).

[12] O. Eytan, A. Jaffa, J. Har-Toov, E. Dalach, and D. Elad, "Dynamics of the intrauterine fluid-wall interface," Ann. Biomed. Eng. **27**, 372 (1999).

[13] L. Fauci, "Peristaltic pumping of solid particles," Comput. Fluids **21**, 583 (1992).

[14] C. Pozrikidis, "A study of peristaltic flow," J. Fluid Mech. **180**, 515 (1987).

[15] S. Usha and A. Rao, "Peristaltic transport of a biofluid in a pipe of elliptic cross section," J. Biomech. **28**, 45 (1995).

[16] R. Cortez, "The method of regularized Stokeslets," SIAM J. Sci. Comput. **23**, 1204 (2001).

[17] R. Cortez, L. Fauci, and A. Medovikov, "The method of regularized Stokeslets in three dimensions: Analysis, validation, and application to helical swimming," Phys. Fluids **17**, 031504 (2005).

[18] E. Bouzarth and M. L. Minion, "A multirate time integrator for regularized Stokeslets," J. Comput. Phys. **229**, 4208 (2010).

[19] L. Cisneros, J. Kessler, R. Ortiz, R. Cortez, and M. Bees, "Unexpected bipolar flagellar arrangements and long-range flows driven by bacteria near solid boundaries," Phys. Rev. Lett. **101**, 168102 (2008).

[20] N. Cogan and S. Chellam, "Regularized Stokeslets solution for 2-d flow in dead-end microfiltration: Application to bacterial deposition and fouling," J. Membr. Sci. **318**, 379 (2008).

[21] E. Gillies, R. Cannon, R. Green, and A. Pacey, "Hydrodynamic propulsion of human sperm," J. Fluid Mech. **625**, 445 (2009).

[22] H. Nguyen, R. Ortiz, R. Cortez, and L. Fauci, "The action of waving cylindrical rings in a viscous fluid," J. Fluid Mech. **671**, 574 (2011).

[23] B. Qian, H. Jiang, D. Gagnon, K. Breuer, and T. Powers, "Minimal model for synchronization induced by hydrodynamic interactions," Phys. Rev. E **80**, 061919 (2009).

[24] D. Smith, "A boundary element regularized Stokeslet method applied to cilia- and flagella-driven flow," Proc. R. Soc. A **465**, 3605 (2009).

[25] O. Eytan and D. Elad, "Analysis of intra-uterine fluid motion induced by uterine contractions," Bull. Math. Biol. **61**, 221 (1999).

[26] L. Bursztyn, O. Eytan, A. Jaffa, and D. Elad, "Modeling myometrial smooth muscle contraction," Ann. N. Y. Acad. Sci. **1101**, 110 (2007).

[27] C. Peskin, "The immersed boundary method," Acta. Numer. **11**, 479 (2002).

[28] R. Dillon and L. Fauci, "An integrative model of internal axoneme mechanics and external fluid dynamics in ciliary beating," J. Theor. Biol. **207**, 415 (2000).

[29] H. Flores, E. Lobaton, S. Mendez-Diez, S. Tlupova, and R. Cortez, "A study of bacterial flagellar bundling," Bull. Math. Biol. **67**, 137 (2005).

[30] E. Tytell, C. Hsu, T. Williams, A. Cohen, and L. Fauci, "Interactions between internal forces, body stiffness, and fluid environment in a neuromechanical model of lamprey swimming," Proc. Natl. Acad. Sci. **107**, 19832 (2010).

[31] S. Yaniv, A. Jaffa, O. Eytan, and D. Elad, "Simulation of embryo transport in a closed uterine cavity model," Eur. J. Obstet. Gynecol. Reprod. Biol. **144**, S50 (2009).